Enhanced performance of dye-sensitized solar cells by doping Au nanoparticles into photoanodes: a size effect study†

Qiong Wang,[a] Teera Butburee,[a] Xia Wu,[a] Hongjun Chen,[a] Gang Liu[*b] and Lianzou Wang[*a]

Remarkably increased power conversion efficiency (PCE) of dye-sensitized solar cells (DSSCs) is achieved by addition of small quantities of Au nanoparticles (NPs) into TiO_2 photoanodes. By doping photoanodes with different sizes of Au NPs, the PCE of cells is improved from 9.59% to 10.80% (~13% enhancement). The maximum increases in open-circuit voltage by 6.69% and short-circuit current density by 7.71% are observed. Detailed characterization of photovoltaic characteristics, electron lifetime and recombination resistance indicates the co-contribution of the photocharging effect, plasmonic effect and scattering effect of Au NPs and their dependence on Au NP sizes. The success of this work provides a simple and generally applicable approach to enhance light harvesting and charge separation for DSSCs.

1. Introduction

Since mesoporous TiO_2 nanoparticle films were introduced as photoanodes in dye-sensitized solar cells (DSSCs) by Grätzel *et al.*,[1] considerable effort has been put into the design of photoanodes in addition to dyes,[2,3] electrolytes[4,5] and counter electrodes[6] for high efficiency DSSCs. Limited light harvesting and insufficient charge separation have been the main challenges for photoanodes of DSSCs.[7–9] Generally, light harvesting of a DSSC is determined primarily by the amount of dye adsorbed by photoanodes and the spectral response of the dye molecules.[10,11] Increasing the photoanode thickness improves dye adsorption,[12] but also extends the length of the diffusion path of electrons; as a result, electrons are more likely to be recombined instead of being collected at the electrodes.[13] Therefore, facilitating light harvesting without detriment to charge separation or collection has been the strategic approach to further improve the performance of DSSCs.

Noble metal nanoparticles have been observed to improve light harvesting in thin film solar cells where metal nanoparticles are dispersed as islands.[14] Three methods of light trapping by noble metal nanoparticles in thin film solar cells have been identified, *i.e.*, sub-wavelength scattering elements that trap incident light inside the films, effective 'antennas' that store the incident energy in a localized surface plasmon mode, and surface plasmon polaritons (SPPs) propagating at the metal/semiconductor interface.[15] In addition, noble metal–semiconductor nanocomposites show advantages in facilitating charge separation of photogenerated electron–hole pairs, as observed in dye photodegradation,[16] photoelectrochemical reactions[17,18] and solid state solar cells.[19,20] Therefore, the benefits in light harvesting and charge separation make application of noble metal nanoparticles in DSSCs a promising field of study. Moreover, the plasmonic effect of noble metal nanoparticles can be used to adjust the spectral response of photoanodes. Recently, by tuning the shell thickness of TiO_2 in TiO_2–Au–TiO_2, a multiple core/shell structure, the broadband light harvesting of photoanodes can be significantly enhanced, and panchromatic DSSCs have been proposed.[21] However, to date, the effect of Au nanoparticles (NPs) on a DSSC system has not been systematically studied, and some conclusions are still controversial. The observed increase in photocurrent of DSSCs was attributed partly to the increased amount of dye loading due to the improved surface area contributed by Ag NPs by some studies,[22] but others claimed the reason to the plasmonic effect of noble metal nanoparticles.[23–25] Meanwhile, possible mechanisms of the plasmonic effect of metal nanoparticles in DSSCs remain unclear. The effective distance between absorbed dye molecules and noble metal nanoparticles for plasmon-enhanced photocurrent in DSSCs was reported to be around 5 nm using 36 nm Ag nanoparticles,[26] but it narrowed to no more than 1 nm in the Au@TiO_2 core/shell structure with 5 nm Au nanoparticles as the core.[27] Such different observations may have resulted from the size difference of employed noble metal nanoparticles in two material systems. On the other hand, in

[a] ARC Centre of Excellence for Functional Nanomaterials, School of Chemical Engineering and Australian Institute for Bioengineering and Nanotechnology, The University of Queensland, St Lucia, Brisbane, QLD, 4072, Australia. E-mail: l.wang@uq.edu.au; Fax: +61-6-33654199; Tel: +61-733654218

[b] Shenyang National Laboratory for Materials Science, Institute of Metal Research, Chinese Academy of Sciences, 72 Wenhua RD, Shenyang 110016, China. E-mail: gangliu@imr.ac.cn; Tel: +86-24-23971088

† Electronic supplementary information (ESI) available. See DOI: 10.1039/c3ta12692g

13524 | *J. Mater. Chem. A*, 2013, **1**, 13524–13531

This journal is © The Royal Society of Chemistry 2013

photocatalytic systems, the photocharging effect in the metal–semiconductor system (caused by electron storage in metal nanoparticles) was observed to result in an up-shift of the Fermi level in metal–semiconductor nanocomposites,[28] which has also been found to be strongly dependent on the metal nanoparticle size.[29] In this regard, although improved open-circuit voltage (V_{oc}) caused by the photocharging effect was reported in Au–nanoparticle-incorporated DSSCs,[27] other effects brought about by changes in the Fermi level in photoanodes and size-dependent V_{oc} on metal nanoparticles have so far not been studied. In addition, despite their application in thin film solar cells,[14] photocatalytic systems[30] or photodetectors[31] for light trapping, the scattering effect of noble metal nanoparticles in DSSCs has not been reported yet. Therefore, it is important to clarify the size effect of noble metal nanoparticles on the performance of DSSCs.

In the present study, Au NPs of different sizes are deliberately designed and fabricated. By adding small quantities of 5, 45 and 110 nm Au NPs into TiO_2 paste (0.2 wt% of Au NPs to TiO_2 NPs), contributions of three effects of Au NPs, i.e., photocharging effect, plasmonic effect and scattering effect to the enhanced performance of DSSCs are systematically investigated and clarified. This would make us capable of identifying some key aspects of the enhancement mechanism in DSSCs influenced by Au NPs.

2. Experimental section

2.1. Preparation of Au NPs with well-controlled shapes and sizes

Hydrogen tetrachloroaurate trihydrate ($HAuCl_4 \cdot 3H_2O$, Aldrich, 99.9%), cetyltrimethylammonium bromide (CTAB, Aldrich, 95%), trisodium citrate ($Na_3C_6H_5O_7 \cdot 2H_2O$, ACS reagent, 99.9%), sodium borohydride ($NaBH_4$, Merck), and ascorbic acid ($C_6H_8O_6$, AR) were used as received without further purification. Octahedral Au nanoparticles of 45 nm and 110 nm were prepared by a modified reported method.[32] Briefly, 0.275 g of CTAB was dissolved in 48.5 mL of Milli-Q water. To the solution, 1.25 mL of 0.01 M $HAuCl_4$ and 250 µL of 0.1 M trisodium citrate were respectively added. The solution was transferred to a Teflon-lined autoclave for hydrothermal reaction at 110 °C (36 and 72 hours for 45 ± 1 nm and 110 ± 2 nm sizes respectively). Au NPs of 5.5 ± 0.6 nm were prepared following a method reported earlier.[33] Briefly, 40 mL of aqueous solution containing 0.25 mM $HAuCl_4$ and 0.25 mM trisodium citrate was prepared in a conical flask. Next, 0.6 mL of freshly prepared 0.1 M $NaBH_4$ solution was added to the solution while stirring. Particles of 3.5 ± 0.7 nm were obtained in this solution and were later used as seeds. Growth solution was prepared by dissolving 1.2 g of solid CTAB into 40 mL of 2.5 mM $HAuCl_4$ solution. For preparation of 5.5 ± 0.6 nm Au NPs, 7.5 mL of growth solution was mixed with 0.5 mL of freshly prepared 0.1 M ascorbic acid solution. Then 25 mL of seed solution was added while stirring. Stirring continued for 10 min after the solution turned wine red. The prepared Au NPs with sizes of less than 20 nm were normally spheres instead of showing various shapes like those of 45 nm and 100 nm Au NPs.

2.2. Fabrication of DSSCs

Before incorporation into the DSSCs, Au NPs of different sizes were extracted from aqueous solution to toluene.[33] After centrifugation and purification, Au NPs were blended into TiO_2 (P25, Degussa) and well dispersed in ethanol to make Au NPs distribute uniformly with TiO_2 NPs (0.2 wt% of Au NPs in TiO_2 was applied in all cases). The concentration of Au NPs in TiO_2 was selected based on our previous experiments where DSSCs with different quantities of Au NPs in TiO_2 were studied and their photovoltaic performance was given in Fig. S1 and Table S1.† Pastes with pristine TiO_2 or Au–TiO_2 were prepared by adopting the method in ref. 34 with modifications. First, TiO_2 films were deposited as the bottom layer on the FTO glass plates by the doctor-blade method, which were gradually heated at 550 °C for 30 min. For traditional DSSCs, another layer of the TiO_2 film was deposited, while for Au incorporated DSSCs (Au–TiO_2-DSSCs), the Au–TiO_2 film was deposited on top of the bottom layer of the TiO_2 film and heated over the same heating profile as previously described. The resulting films were dip-coated in the titanium organic sol.[35] The post-treatment of photoanodes was to deposit a thin layer of TiO_2 on the top of TiO_2–Au mesoporous thin films, which was found to slightly increase dye loading but more importantly to protect Au NPs from the corrosion of iodine based electrolyte effectively.[22,23] Then photoanodes were heated at 450 °C for 50 min, and then immersed into 0.5 mM N719 (Dyesol) dye solution in a 1 : 1 (v/v) mixture of acetonitrile (HPLC, Labscan) and tert-butanol (LR, Ajax Chemicals) and kept for 24 h. Subsequently, the dye-sensitized TiO_2 electrode and the Pt-counter electrode (which was self-prepared following the method in ref. 34) were assembled into a sandwich type cell and sealed with a spacer of 30 µm thickness (Surlyn, DuPont) with a drop of I^-/I_3^- organic solvent based electrolyte solution (EL-HPE, Dyesol) introduced via vacuum back-filling.[34]

2.3. Characterization

Sizes and shapes of Au NPs were characterized by transmission electron microscopy (TEM, JEOL 1010 at 100 kV). The absorbance spectra of Au NPs dispersed in water were measured using a UV-Vis spectrometer (Shimadzu UV-2450).

The cross-sectional morphology of the photoanode and its thickness were observed using a scanning electron microscope (SEM, JEOL 6300) and step-profile meter (Veeco Dektak 150), respectively. The photocurrent density–voltage (J–V) curve measurements employed an AM 1.5 solar simulator (Oriel, 91160_1000) equipped with a 300 W xenon light source (Newport, 6258). The light intensity of the solar simulator was adjusted by using a thermal power meter (Newport, 1918-c) with a detector (818P-040-25). J–V curves were obtained by applying an external bias to the cell and measurements were recorded using a Keithley model 2420 digital source meter. The voltage step and delay time of photocurrent were 10 mV and 10 ms, respectively. The incident photon-to-current conversion efficiency (IPCE) was recorded on a Newport 1918-c power meter under the irradiation of a 300 W xenon light tower (Newport, 66902) with an Oriel Cornerstone™ 260 1/4 m monochromator

(Oriel, 74125) in DC mode. A reference scan with the Si detector (Oriel, 71675_710500) was taken prior to the sample measurement where the background can be subtracted. The yields reported were uncorrected for the absorption and scattering of incident light by the glass. Open-circuit voltage decay (OCVD) measurements were performed using a 440B electrochemical workstation (CH Instruments). Electrochemical impedance spectra (EIS) were recorded using a Solartron 1260 under dark conditions at different applied forward bias voltages (*i.e.*, 0.7 V, 0.65 V, 0.6 V, and 0.55 V); the amplitude of the AC signal was 10 mV and the frequency range was $0.1–10^5$ Hz. The collected spectra (Nyquist plots) were fitted using equivalent circuits. The light scattering and absorption properties of the photoanodes were investigated using a UV-Vis spectrometer (Shimadzu UV-2450) with an integrating sphere. The dye uptake capacity was obtained by first soaking electrodes into 0.5 mM N719 solution at room temperature for 24 hours, followed by desorbing in 0.1 M NaOH water–ethanol (v/v = 1 : 1) mixed solution, and then the resultant NaOH solution was analysed by UV-Vis spectroscopy. Finally, the amount of dye loading was calculated using the absorbance *vs.* concentration calibration curve at 533 nm.

3. Results and discussion

3.1. Characterization of Au NPs

Spherical Au NPs of around 5 nm and octahedral Au NPs of around 45 nm and 110 nm were characterized by TEM (Fig. S2†). Fig. 1 presents the UV-Vis absorbance spectra of Au NPs dispersed in water. The feature absorbance peaks of Au NPs exhibit the localized surface plasmon resonance (LSPR) property.[36] Red shifts in absorbance peaks of Au NPs are observed as particles grow bigger, which can be attributed to the dielectric constant that becomes size-dependent when particle sizes are much smaller than the wavelength of the exciting radiation.[36,37] It is worth noting that the absorbance peak of Au NPs of ~45 nm has the maximum overlap of that of dye N719 in ethanol compared to Au NPs of ~5 nm and ~110 nm.
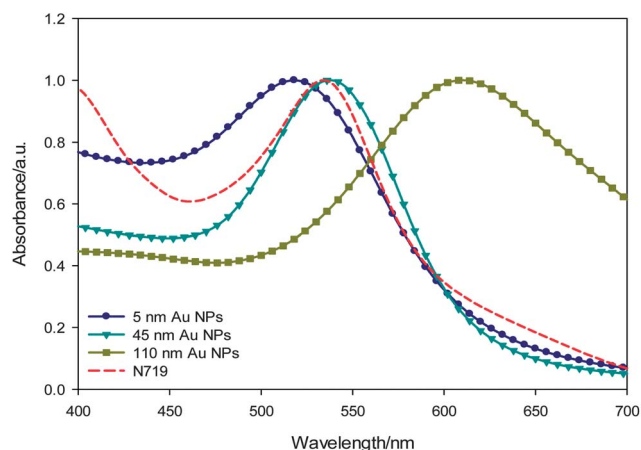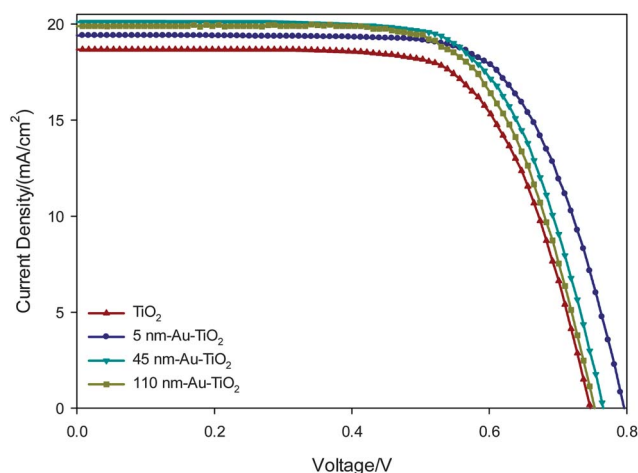
3.2. Photovoltaic characteristics of DSSCs

The cross-sectional image of the Au–TiO$_2$ photoanode is characterized by SEM as shown in Fig. S3a,† and its film thickness of around 20 μm is verified using a step-profile meter (Veeco Dektak 150 surface profilometer, Fig. S3b†). However, we failed to identify the distribution of Au NPs in photoanodes due to their extremely small concentration (SEM 6300 equipped with an EDAX detector). *J*–*V* curves of all DSSCs are shown in Fig. 2 while their photovoltaic and dye adsorption characteristics are summarized in Table 1. It can be seen that the power conversion efficiency (PCE) is improved from 9.59% of TiO$_2$-DSSCs to 10.80%, 10.52%, and 10.20% for 5 nm Au–TiO$_2$-DSSCs, 45 nm Au–TiO$_2$-DSSCs and 110 nm Au–TiO$_2$-DSSCs, respectively. These correspond to 12.6%, 10.0% and 6.4% improvements, respectively. Interestingly, the improved performance of 45 nm Au–TiO$_2$ DSSCs and 110 nm Au–TiO$_2$-DSSCs mainly benefit from the increased short-circuit photocurrent density (J_{sc}) while the efficiency enhancement of 5 nm Au–TiO$_2$ DSSCs comes more from the enhanced open-circuit voltage (V_{oc}) as presented clearly in Fig. 2. Since all the DSSCs were prepared under the same conditions with only variation of the particle size of 0.2 wt% Au NPs, the significant role of Au NPs is remarkable while further investigation is needed to fundamentally understand the reasons.

It is clear from Table 1 that V_{oc} of Au–TiO$_2$-DSSCs increases as particle sizes of Au NPs decrease, with an impressive V_{oc} of 0.797 V for 5 nm Au–TiO$_2$-DSSCs. The increase in V_{oc} has been attributed to the photocharging effect, caused by the electron storage in metal NPs, which drives the Fermi level to more negative potentials.[27] In our study, the size-dependent change of V_{oc} of Au–TiO$_2$-DSSCs can be reasonably explained by the size-dependent shift of the Fermi level of the Au–TiO$_2$ NCs over pristine TiO$_2$ NPs,[29] where the smaller the sizes of Au NPs, the more the up-shifts of the Fermi level in Au–TiO$_2$ NCs. Nevertheless, an increase of 50 mV in V_{oc} exhibited by our 5 nm Au–TiO$_2$-DSSCs is still quite significant, which indicates that other factors may be caused by the up-shift of the Fermi level and they may in turn benefit V_{oc}, *e.g.* easier charge separation, longer

Fig. 1 UV-Vis absorbance spectra of different-sized Au NPs in water (solid line) and N719 dye in ethanol (dashed line).

Fig. 2 *J*–*V* curves of Au–TiO$_2$-DSSCs and TiO$_2$-DSSCs under AM-1.5G one sun irradiation.

13526 | *J. Mater. Chem. A*, 2013, **1**, 13524–13531

This journal is © The Royal Society of Chemistry 2013

Table 1 Comparison of photovoltaic properties and dye loading of Au–TiO$_2$-DSSCs and TiO$_2$-DSSCs. Measurements were performed under AM 1.5G one sun (light intensity: 100 mW cm^{-2}) and the active area was *ca.* 0.16 cm^2 for all of the DSSCs. The data are based on the average value of 8 cells for each sample[a]

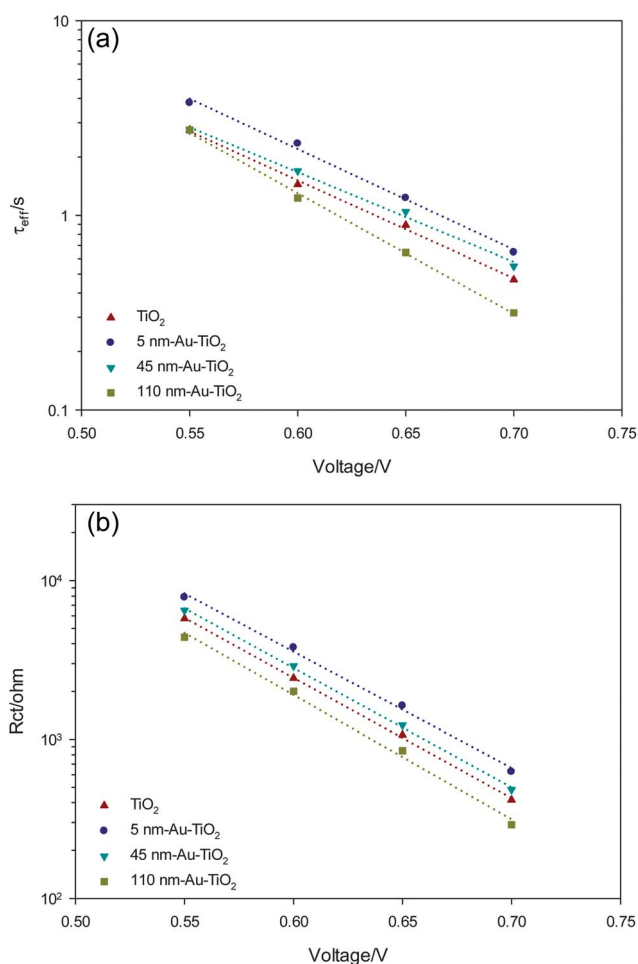| Samples	FF	V_{oc} [V]	J_{sc} [mA cm^{-2}]	η [%]	Thickness [μm]	Absorbed dye [× 10^{-7} mol cm^{-2}]
TiO$_2$	0.688	0.747	18.67	9.59	19.5 ± 0.5	1.418
5 nm Au–TiO$_2$	0.698	0.797	19.40	10.80	19.8 ± 0.5	1.432
45 nm Au–TiO$_2$	0.685	0.764	20.11	10.52	19.6 ± 0.5	1.424
110 nm Au–TiO$_2$	0.681	0.753	19.89	10.20	20.5 ± 0.5	1.428

[a] Dye-absorbed films with a dimension of *ca.* 3 cm^2 were used for estimating the dye uptake.

electron lifetime and higher recombination resistance, as will be discussed later.

3.3. Electrochemical impedance spectroscopy (EIS) analysis

In order to study the charge recombination and electron transport properties of Au–TiO$_2$ photoanodes in DSSCs, EIS was measured in the dark to avoid the plasmonic effect of Au NPs excited under illumination. The measured and fitted Nyquist plots of all samples at a forward bias voltage of 0.6 V are analysed using Bisquert's transmission line model[38,39] in Fig. S4a

Fig. 3 (a) Electron effective lifetime (τ_{eff}) as a function of applied forward bias. (b) Recombination resistance (R_{ct}) at TiO$_2$/electrolyte interfaces as a function of applied forward bias.

and b† and the Nyquist plots are illustrated in Fig. S5.† Parameters such as electron effective lifetime (τ_{eff}) and recombination resistance (R_{ct}) of samples are deduced from the Nyquist plots as explained in Fig. S4c† and are plotted as a function of applied forward bias as shown in Fig. 3. The electron effective lifetime (τ_{eff}) exhibits an approximate exponential dependence on applied bias as expected.[40] Under the same bias, it is clear that DSSCs of 5 nm Au–TiO$_2$ and 45 nm Au–TiO$_2$ photoanodes have a longer electron effective lifetime than that of pristine TiO$_2$-DSSCs, which indicates longer existence of free electrons in the conduction band of TiO$_2$ NPs and thus implies less chances of recombination occurring during diffusion of electrons through photoanodes. This speculation is further supported by the recombination resistance (R_{ct}) shown in Fig. 3b. The exponential dependence of recombination resistance on bias is observed.[41] Larger recombination resistance in 5 nm Au–TiO$_2$-DSSCs and 45 nm Au–TiO$_2$-DSSCs indicates that interfacial recombination reactions are efficiently suppressed compared with pristine TiO$_2$-DSSCs. Fig. 3 shows that both the electron effective lifetime and the recombination resistance decrease with the increase of Au NP sizes. The observed dependence of τ_{eff} and R_{ct} in Au–TiO$_2$-DSSCs on sizes of Au NPs is believed to be caused by the size-dependent shift of the quasi-Fermi level of Au–TiO$_2$ NCs.
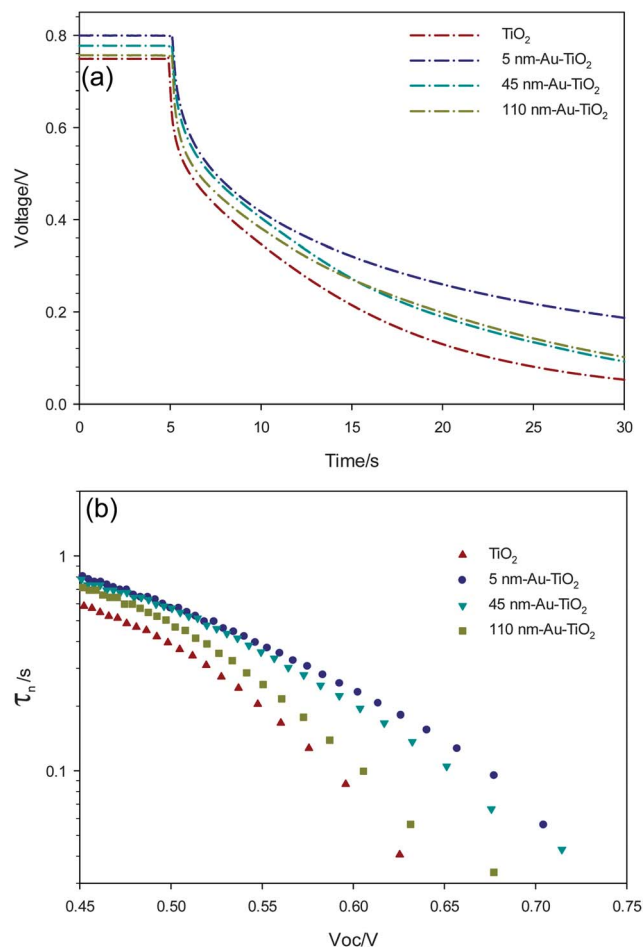
3.4. Open-circuit voltage decay (OCVD) measurement

The OCVD measurement is known as a complementary tool to EIS, as it measures free electrons in the semiconductor conduction band evolved from constant at a nonequilibrium steady-state to the dark equilibrium state as a result of charge recombination.[42] As shown in Fig. 4, the decay of V_{oc} is slower in Au–TiO$_2$-DSSCs than that in TiO$_2$-DSSCs, which indicates a slower charge recombination process in Au–TiO$_2$-DSSCs. The electron lifetime (τ_n) as a function of the quasi-Fermi level can be given by the reciprocal of the derivative of the decay curve normalized by the thermal voltage as defined in the following,[42,43]

$$\tau_n = -\frac{k_B T}{d}\left(\frac{dV_{oc}}{dt}\right)^{-1} \tag{1}$$
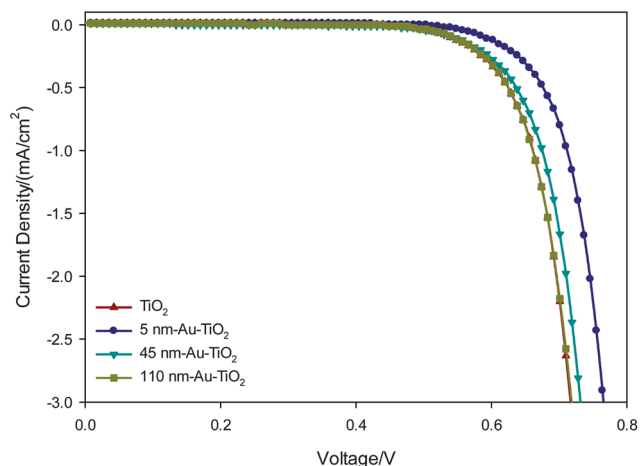
where $k_B T$ is the thermal energy, e is the positive elementary charge, and open-circuit voltage V_{oc} can be expressed as $(E_{Fn} - E_{F0})/e$, corresponding to the increase of the quasi-Fermi level of the semiconductor (E_{Fn}) with respect to the dark value

Fig. 5 Dark current potential scans of Au–TiO$_2$-DSSCs and TiO$_2$-DSSCs.

Fig. 4 (a) Open-circuit voltage decay curves of Au–TiO$_2$-DSSCs and TiO$_2$-DSSCs. Generally, the final region of decay at V_{oc} of 50 mV or less is poorly resolved in the current setup and thus is neglected.[43] (b) Electron lifetime extracted from $V_{oc}(t)$ (Fig. 4a) as a function of V_{oc}. Electron lifetime measured by the OCVD technique is different from that measured by EIS, as the former corresponds to an average of characteristic times for survival of free and trapped electrons while the latter characterizes the life-spans of free carriers in the conduction band of a semiconductor.

physically blended with TiO$_2$ NPs, as a result, the surface states of TiO$_2$ NPs can be affected by the incorporation of Au NPs, but the bulk traps inside the TiO$_2$ NPs are very likely to be kept intact. Therefore, the incorporation of Au NPs into TiO$_2$ NPs assists in the elimination of surface traps in the semiconductor, leading to reduced charge recombination as consistent with the recombination resistance obtained from the EIS analysis.

3.5. Dark current potential scans

The overall competition between electrons to be transported in mesoporous TiO$_2$ films or collected at the conductive glass and regeneration of I$_3^-$ ions in the electrolyte can be reflected in dark current potential scans.[7] As shown in Fig. 5, the dark current onset of Au–TiO$_2$-DSSCs is shifted to higher potentials with the decrease of Au NP sizes. Among all the cells, 5 nm Au–TiO$_2$-DSSCs exhibit a higher potential at the dark current onset and generate a smaller dark current at the same potential above 0.6 V, which indicates less suffering from charge carrier recombination.

It can be concluded that the photocharging effect that is strongly dependent on sizes of Au NPs results in size-dependent shifts of the Fermi level, and therefore the observed V_{oc} is also strongly dependent on the sizes of Au NPs, where 5 nm Au–TiO$_2$-DSSCs exhibit the biggest increase of 6.7% in V_{oc} due to the maximum up-shifts of the Fermi level in Au–TiO$_2$ photoanodes. Moreover, it is observed that an up-shift of the Fermi level in Au–TiO$_2$ photoanodes results in longer electron lifetime and higher recombination resistance, which benefits charge transport and collection at the electrodes, and thus in turn improves V_{oc} in Au–TiO$_2$-DSSCs. This also reflects in the higher fill factor exhibited in 5 nm Au–TiO$_2$-DSSCs.

3.6. Photocurrent characteristics of DSSCs

As shown in Fig. 2, J_{sc} values of DSSCs increase from 18.67 mA cm^{-2} of TiO$_2$-DSSCs to 19.40 mA cm^{-2} of 5 nm Au–TiO$_2$-DSSCs, 20.11 mA cm^{-2} of 45 nm Au–TiO$_2$-DSSCs and 19.89 mA cm^{-2} of 110 nm Au–TiO$_2$-DSSCs. The increase in J_{sc} of DSSC incorporated noble metal nanoparticles has been discussed earlier.[24,44]

(E_{F0}) which is equal to the electrolyte redox energy ($E_{F0} = E_{redox}$). Note that the measured lifetime (τ_n) does not in general correspond to the free carrier lifetime (as measured by EIS) but consists of an average of characteristic times for survival of free and trapped electrons. The electron lifetime (τ_n) calculated from $V_{oc}(t)$ (given in Fig. 4a) is depicted in Fig. 4b. The decay of the electron lifetime over different potentials from 0.5 V to 0.65 V happens to all samples and presents a size-dependence for Au–TiO$_2$-DSSCs which is determined by the quasi-Fermi level of Au–TiO$_2$ NCs as implied in eqn (1). It is observed that the distribution of $\tau_n(E_F)$ of TiO$_2$-DSSCs is more shallow than that in Au–TiO$_2$-DSSCs, which indicates a smaller character parameter of surface traps than that of bulk traps ($T_1 < T_0$) in TiO$_2$ NPs.[42] As a result, less concentration of surface traps in the energy levels near E_c (lower edge of the conduction band) is expected in Au–TiO$_2$ NCs than that in TiO$_2$ NPs if we assume the bulk traps existed in all samples are nearly the same. Actually this assumption would be genuine in our system, since Au NPs are

13528 | *J. Mater. Chem. A*, 2013, **1**, 13524–13531

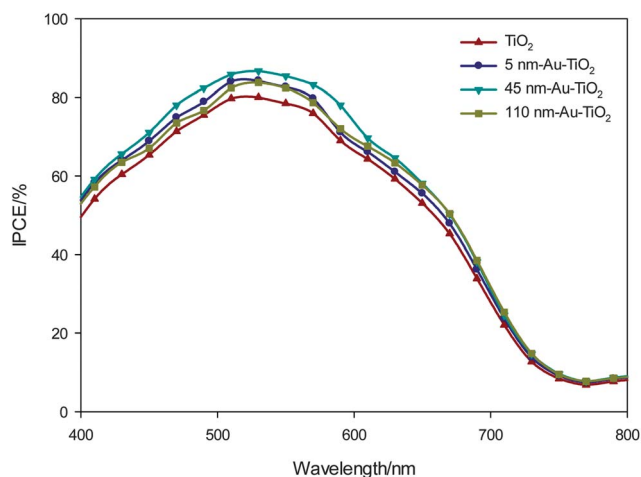This journal is © The Royal Society of Chemistry 2013

Fig. 6 IPCE spectra of Au–TiO$_2$-DSSCs and TiO$_2$-DSSCs.

Some reports attributed this to the LSPR of Au NPs,[25] while others ascribed half of this to increased dye loading in metal–TiO$_2$ photoanodes.[22] Here, the dye adsorption of Au–TiO$_2$ photoanodes and TiO$_2$ photoanodes is measured and summarized in Table 1. It shows that the quantity of dye adsorbed on Au–TiO$_2$ photoanodes is nearly the same as that on pristine photoanodes. Even though it is speculated that the photoanodes doped by small noble metal nanoparticles will enhance the surface area, and thus improve the dye adsorption,[22] given the very small amount of Au NPs employed in our system, this effect is negligibly observable. The changes in J_{sc} are further analysed by incident photon-to-current conversion efficiency (IPCE) measurement (Fig. 6). IPCE (λ) is determined by light harvesting efficiency, electron injection and charge collection efficiency,[1] and therefore provides more insight into the electron-involved processes after the photo-excitation of dye sensitizers.[45,46] The highest IPCE is achieved by 45 nm Au–TiO$_2$-DSSCs, which is in good agreement with the observed J_{sc}. It is believed that the significant increase in IPCE comes mainly from the improved light harvesting efficiency. As we mentioned earlier, the absorbance peak of 45 nm Au NPs has the maximum overlap of that of N719 (Fig. 1), thus the plasmon resonant effect between 45 nm Au NPs and N719 dye molecules can be most strongly strengthened,[36,37,47,48] which contributes to the enhanced light intensity in the vicinity of Au NPs,[15] and thus the improved light absorbance of dye molecules, and increased J_{sc}.

On the other side, in 5 nm Au–TiO$_2$-DSSCs, the plasmon resonance between N719 dye and 5 nm Au NPs is not as strong as that of 45 nm Au NPs, which results in smaller increase in light harvesting efficiency, while the improved electron collection efficiency originating from a longer electron lifetime in 5 nm Au–TiO$_2$ photoanodes, as discussed above, devotes considerably to IPCE and J_{sc} improvement. The stronger charging effect but weaker plasmonic effect of 5 nm Au NPs, while the weaker charging effect but stronger plasmonic effect of 45 nm Au NPs, observed in our study, also explains well that the effective distance of the plasmonic effect of 5 nm Au NPs is no more than 1 nm while the distance increases to 4.8 nm for 36 nm Ag NPs.[26,27] However, in 110 nm Au–TiO$_2$-DSSCs, the

electron effective lifetime and recombination resistance are slightly lower than that of pristine TiO$_2$-DSSCs as observed from EIS and OCVD measurements, which can be ascribed to the slightly bigger film thickness of 110 nm Au–TiO$_2$ photoanodes than that of pristine TiO$_2$ photoanodes, resulting in a smaller fill factor of 110 nm Au–TiO$_2$-DSSCs as shown in Table 1. Therefore, the electron collection efficiency in 110 nm Au–TiO$_2$-DSSCs cannot be the contributor to the increased IPCE. Owing to the small overlap of absorbance spectra of 110 nm Au NPs and N719, the weakened plasmon resonance cannot be the primary contributor either. As a result, we further explored the possible reasons that brought about the increased IPCE and J_{sc} in 110 nm Au–TiO$_2$-DSSCs in the next section.

3.7. Diffuse reflectivity

It was reported that the magnitude of visible light scattering by Au NPs of around 80 nm was comparable to the scattering from the much larger 300 nm polystyrene nanoparticles.[47] To verify the light scattering contribution of Au NPs, the diffused reflectance spectra of photoanodes were measured (Fig. 7a). It can be seen that photoanodes of 110 nm Au–TiO$_2$ exhibit the highest reflectance from 450 nm to 800 nm. After dye adsorption, the reflectance of the films is decreased drastically in the
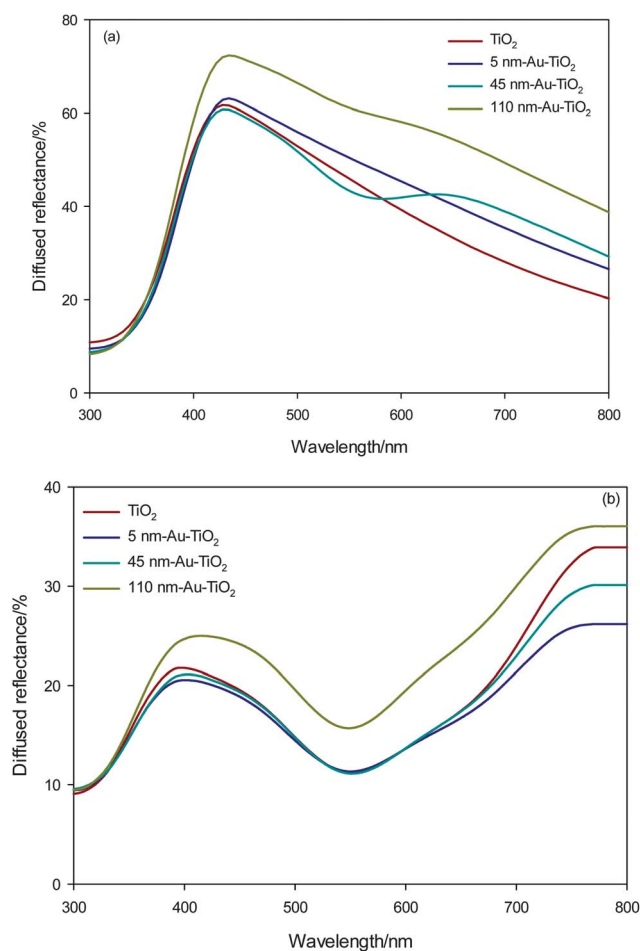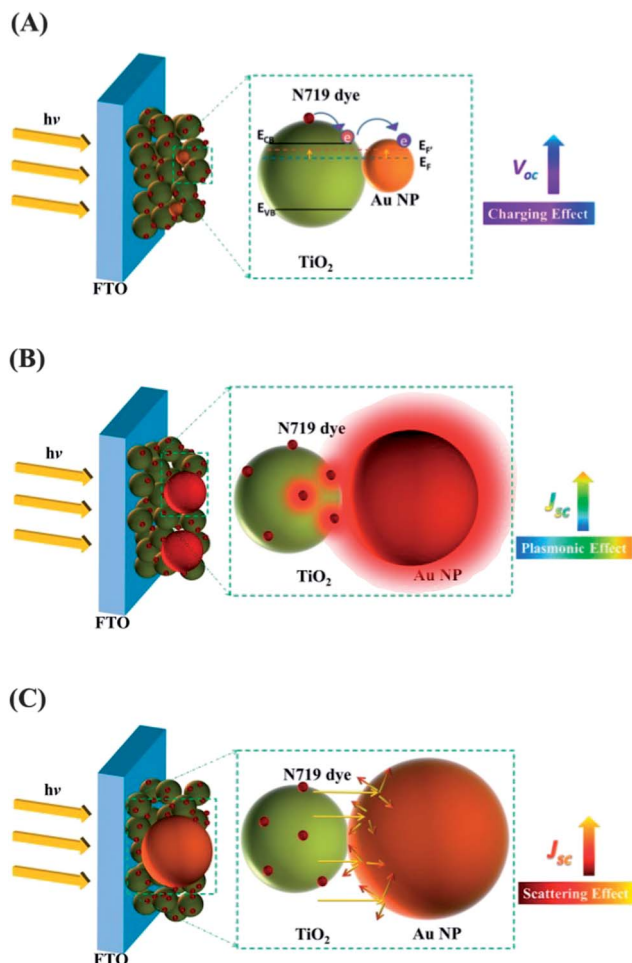

Fig. 7 Diffused reflectance spectra of photoanodes before (a) and after (b) dye loading.

Scheme 1 (A) Schematic illustration of the photocharging effect of 5 nm Au NPs, (B) plasmonic effect of 45 nm Au NPs, and (C) scattering effect of 110 nm Au NPs.

short wavelength ranging from 400 to 600 nm (Fig. 7b), which is mainly attributed to light absorbance of dye molecules. However, in the longer wavelength region, the dye-loaded 110 nm Au–TiO$_2$ photoanodes still retain a substantially higher reflectance than that of the pristine TiO$_2$ film. The enhanced light scattering observed for DSSCs of 110 nm Au NPs also presents a clearly visualized impact in the normalized IPCE spectra of DSSCs shown in Fig. S6† where an enhancement in light conversion efficiency from 550 nm until far in the absorption tail (up to 750 nm) is exhibited, which further supports our argument that the 6.5% increase in J_{sc} for 110 nm Au–TiO$_2$-DSSCs compared with TiO$_2$-DSSCs comes primarily from superior light scattering by 110 nm Au NPs. However, the higher IPCE in the same wavelength range of Au–TiO$_2$-DSSCs with 5 nm or 45 nm Au NPs is likely to be resulted from the localized surface plasmon resonance (LSPR),[49] which is supported by the slightly enhanced absorbance of 5 nm/45 nm Au–TiO$_2$-photoanodes in the wavelength range of 550–700 nm as shown in Fig. S7.†

Based on our experimental results and analysis, the size effect of Au NPs on the performance of DSSCs is summarized in Scheme 1. Au NPs of very small size, i.e. 5 nm, are excited by

light of short-wavelength and high energy, and present the strongest the photocharging effect, which results in a dominant enhancement in V_{oc}. Au NPs of medium size, i.e. 45 nm, interact more with visible light of mid-wavelength, and exhibit the most powerful plasmonic effect, which generates a significant increase in J_{sc}. Au NPs of large size, i.e., 110 nm, scatter light in long wavelengths, and show the strongest scattering effect, which contributes to the apparent improvement in J_{sc}.

4. Conclusions

In summary, the advantages of Au–TiO$_2$-DSSCs over TiO$_2$-DSSCs have been successfully demonstrated by tuning Au NP sizes from 5 nm to 110 nm. It is revealed that the photocharging effect, plasmonic effect and scattering effect of Au NPs co-exist in DSSCs but are selectively dominant in different sizes. As a consequence, an efficiency of 10.8% is achieved by 5 nm Au–TiO$_2$-DSSCs with enhancement in V_{oc}, J_{sc} and fill factor. These observations provide a very useful design guideline for achieving efficient light harvesting and charge separation in DSSCs.

Acknowledgements

Notes and references

1 B. Oregan and M. Grätzel, *Nature*, 1991, **353**, 737–740.
2 A. Yella, H.-W. Lee, H. N. Tsao, C. Yi, A. K. Chandiran, M. K. Nazeeruddin, E. W.-G. Diau, C.-Y. Yeh, S. M. Zakeeruddin and M. Grätzel, *Science*, 2011, **334**, 629–634.
3 A. Kojima, K. Teshima, Y. Shirai and T. Miyasaka, *J. Am. Chem. Soc.*, 2009, **131**, 6050–6051.
4 I. Chung, B. Lee, J. He, R. P. H. Chang and M. G. Kanatzidis, *Nature*, 2012, **485**, 486–489.
5 X. Liu, W. Zhang, S. Uchida, L. Cai, B. Liu and S. Ramakrishna, *Adv. Mater.*, 2010, **22**, E150–E155.
6 O. K. Varghese, M. Paulose and C. A. Grimes, *Nat. Nanotechnol.*, 2009, **4**, 592–597.
7 S. Ito, P. Liska, P. Comte, R. L. Charvet, P. Pechy, U. Bach, L. Schmidt-Mende, S. M. Zakeeruddin, A. Kay, M. K. Nazeeruddin and M. Gratzel, *Chem. Commun.*, 2005, 4351–4353.
8 F. Huang, D. Chen, X. L. Zhang, R. A. Caruso and Y.-B. Cheng, *Adv. Funct. Mater.*, 2010, **20**, 1301–1305.
9 Y. Bai, H. Yu, Z. Li, R. Amal, G. Q. Lu and L. Wang, *Adv. Mater.*, 2012, **24**, 5850–5856.
10 X. Wu, G. Q. Lu and L. Wang, *Energy Environ. Sci.*, 2011, **4**, 3565–3572.
11 J. Y. Liao, B. X. Lei, D. B. Kuang and C. Y. Su, *Energy Environ. Sci.*, 2011, **4**, 4079–4085.
12 M. Gratzel, S. Ito, P. Chen, P. Comte, M. K. Nazeeruddin, P. Liska and P. Pechy, *Prog. Photovoltaics*, 2007, **15**, 603–612.

13 A. Hagfeldt, G. Boschloo, L. C. Sun, L. Kloo and H. Pettersson, *Chem. Rev.*, 2010, **110**, 6595–6663.

14 V. E. Ferry, L. A. Sweatlock, D. Pacifici and H. A. Atwater, *Nano Lett.*, 2008, **8**, 4391–4397.

15 H. A. Atwater and A. Polman, *Nat. Mater.*, 2010, **9**, 205–213.

16 N. G. Park, J. van de Lagemaat and A. J. Frank, *J. Phys. Chem. B*, 2000, **104**, 8989–8994.

17 Y. Tian and T. Tatsuma, *J. Am. Chem. Soc.*, 2005, **127**, 7632–7637.

18 H. M. Chen, C. K. Chen, C.-J. Chen, L.-C. Cheng, P. C. Wu, B. H. Cheng, Y. Z. Ho, M. L. Tseng, Y.-Y. Hsu, T.-S. Chan, J.-F. Lee, R.-S. Liu and D. P. Tsai, *ACS Nano*, 2012, **6**, 7362–7372.

19 Y. Takahashi and T. Tatsuma, *Appl. Phys. Lett.*, 2011, **99**, 182110.

20 P. Reineck, G. P. Lee, D. Brick, M. Karg, P. Mulvaney and U. Bach, *Adv. Mater.*, 2012, **24**, 4750–4755.

21 M. Zukalová, A. Zukal, L. Kavan, M. K. Nazeeruddin, P. Liska and M. Grätzel, *Nano Lett.*, 2005, **5**, 1789–1792.

22 N. C. Jeong, C. Prasittichai and J. T. Hupp, *Langmuir*, 2011, **27**, 14609–14614.

23 S. D. Standridge, G. C. Schatz and J. T. Hupp, *Langmuir*, 2009, **25**, 2596–2600.

24 J. F. Qi, X. N. Dang, P. T. Hammond and A. M. Belcher, *ACS Nano*, 2011, **5**, 7108–7116.

25 M. D. Brown, T. Suteewong, R. S. S. Kumar, V. D'Innocenzo, A. Petrozza, M. M. Lee, U. Wiesner and H. J. Snaith, *Nano Lett.*, 2011, **11**, 438–445.

26 S. D. Standridge, G. C. Schatz and J. T. Hupp, *J. Am. Chem. Soc.*, 2009, **131**, 8407–8409.

27 H. Choi, W. T. Chen and P. V. Kamat, *ACS Nano*, 2012, **6**, 4418–4427.

28 V. Subramanian, E. E. Wolf and P. V. Kamat, *J. Phys. Chem. B*, 2003, **107**, 7479–7485.

29 V. Subramanian, E. E. Wolf and P. V. Kamat, *J. Am. Chem. Soc.*, 2004, **126**, 4943–4950.

30 A. Nattestad, A. J. Mozer, M. K. R. Fischer, Y. B. Cheng, A. Mishra, P. Bauerle and U. Bach, *Nat. Mater.*, 2010, **9**, 31–35.

31 F. P. G. de Arquer, F. J. Beck, M. Bernechea and G. Konstantatos, *Appl. Phys. Lett.*, 2012, **100**, 043101.

32 C. C. Chang, H. L. Wu, C. H. Kuo and M. H. Huang, *Chem. Mater.*, 2008, **20**, 7570–7574.

33 Y. D. Wang, C. Y. Zhao, D. Qin, M. X. Wu, W. Liu and T. L. Ma, *J. Mater. Chem.*, 2012, **22**, 22155–22159.

34 S. Ito, T. N. Murakami, P. Comte, P. Liska, C. Gratzel, M. K. Nazeeruddin and M. Gratzel, *Thin Solid Films*, 2008, **516**, 4613–4619.

35 H. Yu, S. Zhang, H. Zhao, B. Xue, P. Liu and G. Will, *J. Phys. Chem. C*, 2009, **113**, 16277–16282.

36 S. Link and M. A. El-Sayed, *J. Phys. Chem. B*, 1999, **103**, 4212–4217.

37 K. L. Kelly, E. Coronado, L. L. Zhao and G. C. Schatz, *J. Phys. Chem. B*, 2003, **107**, 668–677.

38 J. Bisquert, *Phys. Chem. Chem. Phys.*, 2000, **2**, 4185–4192.

39 F. Fabregat-Santiago, J. Bisquert, G. Garcia-Belmonte, G. Boschloo and A. Hagfeldt, *Sol. Energy Mater. Sol. Cells*, 2005, **87**, 117–131.

40 J. P. Gonzalez-Vazquez, J. A. Anta and J. Bisquert, *J. Phys. Chem. C*, 2010, **114**, 8552–8558.

41 Q. Wang, S. Ito, M. Gratzel, F. Fabregat-Santiago, I. Mora-Sero, J. Bisquert, T. Bessho and H. Imai, *J. Phys. Chem. B*, 2006, **110**, 25210–25221.

42 J. Bisquert, A. Zaban, M. Greenshtein and I. Mora-Sero, *J. Am. Chem. Soc.*, 2004, **126**, 13550–13559.

43 A. Zaban, M. Greenshtein and J. Bisquert, *ChemPhysChem*, 2003, **4**, 859–864.

44 H. Chen, M. G. Blaber, S. D. Standridge, E. J. DeMarco, J. T. Hupp, M. A. Ratner and G. C. Schatz, *J. Phys. Chem. C*, 2012, **116**, 10215–10221.

45 E. J. W. Crossland, N. Noel, V. Sivaram, T. Leijtens, J. A. Alexander-Webber and H. J. Snaith, *Nature*, 2013, **495**, 215–219.

46 A. C. Fisher, L. M. Peter, E. A. Ponomarev, A. B. Walker and K. G. U. Wijayantha, *J. Phys. Chem. B*, 2000, **104**, 949–958.

47 P. K. Jain, K. S. Lee, I. H. El-Sayed and M. A. El-Sayed, *J. Phys. Chem. B*, 2006, **110**, 7238–7248.

48 M. M. Alvarez, J. T. Khoury, T. G. Schaaff, M. N. Shafigullin, I. Vezmar and R. L. Whetten, *J. Phys. Chem. B*, 1997, **101**, 3706–3712.

49 E. Thimsen, F. Le Formal, M. Gratzel and S. C. Warren, *Nano Lett.*, 2011, **11**, 35–43.

This journal is © The Royal Society of Chemistry 2013

J. Mater. Chem. A, 2013, **1**, 13524–13531 | **13531**